Wetting behavior in the Co-Pt system

Y. Le Bouar, A. Loiseau, A. Finel, and F. Ducastelle
Laboratoire d'Etude des Microstructures (LEM), ONERA-CNRS, Boîte Postale 72, 92322 Châtillon Cedex, France
(Received 9 July 1999)

In the Co-Pt system, a simple cooling experiment can drive a sample ordered in the cubic $L1_2$ structure (Cu_3Au type) close to the two-phase region involving $L1_2$ and the tetragonal $L1_0$ (CuAu type) structure. Using transmission electron microscopy observations, we show that the antiphase boundaries (APB's) in the $L1_2$ structure are decorated by the $L1_0$ structure and that the $L1_0$ variant formed during this wetting process is related to the characteristics of the APB. The $L1_0$ tetragonal axis is normal to the displacement vector of the APB and the translational variant ensures the continuity of the platinum-rich cubic planes between the bulk and the wetting structure. To understand this peculiar wetting process, we develop different theoretical approaches based on a microscopic Ising model on the fcc lattice with interactions up to the second nearest neighbors. At 0 K, the model accounts for the observed selectivity of the wetting process. Then, using a mean field approach, our model predicts the wetting by the $L1_0$ structure at finite temperature, with a selectivity similar to that observed in the Co-Pt samples. Furthermore, the usual logarithmic divergence of the width of the wetting layer with respect to the excess free energy still holds. Finally, we use a general phenomenological Landau approach, where the symmetries of the fcc lattice and of the (vectorial) order parameter are taken into account, to show that the width of the wetting layer is very sensitive to the orientation of the APB. This phenomenological approach makes it clear also that the wetting of the APB in the $L1_2$ structure by the $L1_0$ phase, although observed here, is not unavoidable theoretically, which is not the case when the relevant order parameter is scalar.

I. INTRODUCTION

The wetting phenomenon of antiphase boundaries (APB's) by the disordered solid solution has been a focus of intensive research, both theoretically[1–4] and experimentally;[5–7] for general reviews see Refs. 8–10. Much less is known concerning the wetting phenomenon by an ordered phase, where new features are expected due to the degeneracy of the ordered structure. Indeed, the system may choose only one or several variants of the ordered phase to be formed along the APB. Furthermore, as the width of the wetting layer increases, the accomodation of the elastic strain due to the misfit between the bulk structure and the variants of the new ordered phase may lead to a nontrivial behavior of the APB. In this paper, we focus on the very first steps of such a wetting phenomenon, when the width of the wetting layer is small enough to neglect the influence of elastic strains. The consequences of the misfit between the bulk and the wetting structure on the microstructure will be discussed elsewhere.

In the first part of this paper, we present the results of a wetting phenomenon by an ordered phase in the Co-Pt system. Platinum rich Co-Pt alloys are chemically disordered on a fcc lattice at high temperature and ordered at low temperature according to either a cubic $L1_2$ structure ($CoPt_3$) or a tetragonal $L1_0$ structure (CoPt), depending on the alloy concentration, and there is a narrow concentration range where the two ordered phases coexist at equilibrium. It has been shown in a previous work that the two-phase alloys can be obtained through different ordering reactions from either the disordered state, or the $L1_0$ state, or the $L1_2$ state.[11] We focus here on the transformation path corresponding to a sample initially ordered in the $L1_2$ structure. Using different electron microscope techniques we show first that a wetting layer of $L1_0$ structure appears along the APB of the $L1_2$ phase. Particular attention is paid to the relationship between the initial configuration of the APB and the $L1_0$ variant formed by wetting.

In the following parts of the paper, we develop different theoretical approaches to understand the latter relationship and to test whether the usual qualitative features of the wetting phenomenon by a disordered solid solution still apply to the peculiar wetting phenomenon observed in the Co-Pt system.

II. EXPERIMENTAL PROCEDURE

A. Sample preparation

The procedure followed for the sample preparation is the same as that used in previous works on Co-Pt alloys.[11,12] Alloys containing from 61.5 to 63 % at. Pt were prepared by melting pure Co and pure Pt in an arc furnace in the form of small ingots which were homogenized during two days at 1000 °C under partial He pressure. Thin sheets (150 μm thick) were obtained by rolling and discs where punched out of the sheets, sealed in evacuated quartz tubes under partial He atmosphere, annealed at 930 °C to remove strains induced by rolling, and water quenched. The discs were then annealed according to the following procedure: They were first heated up to 740 °C and then slowly cooled at a rate of 10 or 40 °C/24 h down to the temperature of interest, and finally maintained at this temperature during two to four weeks and quenched. As shown by Leroux *et al.*,[11] this procedure produces large ordered domains of the different phases at any temperature. Finally, the samples were thinned to electron transparency by Ar ion thinning and the surfaces were

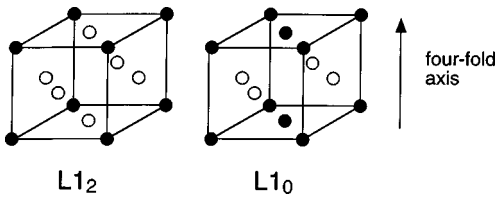

FIG. 1. $L1_2$ and $L1_0$ structures.

cleaned in aqua regia to remove the damaged areas produced by the ion bombardment. The microstructure studies were performed by transmission electron microscopy (TEM) with a Jeol 4000FX working at 400 keV.

B. Structures and imaging conditions

The Co-Pt binary compounds are ordered at low temperature on the fcc lattice according to either the simple cubic $L1_2$ structure (Cu_3Au type) or the tetragonal $L1_0$ structure (CuAu type). In the perfect $L1_2$ structure (see Fig. 1), the Co atoms occupy the vertices of the cube and the Pt atoms its face centres. This structure displays four ordered variants separated by three kinds of antiphase boundaries APB, the three possible displacement vectors being $\mathbf{R}_1=\frac{1}{2}[011]$, $\mathbf{R}_2=\frac{1}{2}[101]$, and $\mathbf{R}_3=\frac{1}{2}[110]$. The $L1_0$ structure is formed by alternating (100) planes of cobalt and platinum. The structure is tetragonal and three orientational variants can be formed with two possible translational variants for each of them.

The $L1_2$ and $L1_0$ structures can be distinguished by using the dark field technique in two-beam conditions involving superstructure reflections. This technique also allows us to characterize the displacement vectors of the antiphase boundaries in the pure $L1_2$ phase. The method is here shortly recalled. More details can be found in Refs. 11 and 12. For all the observations, the foil was oriented with a [001] cube axis nearly parallel to the incident beam. This orientation is very convenient since the corresponding zone axis displays the different kinds of superstructure reflections produced by both $L1_2$ and $L1_0$ structures, namely, (100), (010), and (110). Three different dark field (DF) images were obtained with the (120), (210), and (110) reflections. (120) and (210) reflections were used instead of (100) and (010) since they are more easily attained in two-beam conditions.[6,7]

In the kinematic approximation, the DF intensity corresponding to a given structure is proportional to the square of the structure factor. Except for a weak variation of the form factor between the (120), (210) beams and the (110) beam, these three beams have similar structure factors in the $L1_2$ phase. On the other hand, for a given orientation variant of the $L1_0$ structure, the specific form of the structure factor gives rise to extinctions for two beams and the structure factor of the third one is larger than those of $L1_2$. As a consequence, for a given (120), (210), or (110) DF, a $L1_0$ zone appears either black or brighter than the $L1_2$ zones, depending on the orientation of the tetragonal axis. As shown in Table I, this contrast rule allows us to distinguish between the different $L1_0$ orientational variants and the $L1_2$ phase. For convenience, we have introduced in Table I three levels of illumination: Black (extinction), gray ($L1_2$), and white ($L1_0$). This contrast rule has been successfully used to characterize the microstructures of the two-phase $L1_2+L1_0$ Co-Pt alloys.[11,12]

The transmission electron microscopy in superstructure dark field mode also provides a convenient tool for visualizing and characterizing the APB.[6,7] In a dark field image, where we have selected the vector of the reciprocal space **g**, the APB is in contrast unless the displacement vector **R** between the two domains induces a phase shift $\alpha=2\pi\mathbf{g}\cdot\mathbf{r}$ equal to zero modulo 2π. The APB is then out of contrast and cannot be seen in the selected DF. When the APB is in contrast and the two-beam conditions are achieved, the dynamical theory predicts the formation of fringes with a periodicity equal to the extinction length corresponding to the selected beam.[13] In a (110), (210), or (120) dark field image, an APB in contrast appears as a unique black fringe because the extinction length corresponding to these superstructure reflections is larger than the thickness of the Co-Pt sample. The displacement vector is easily determined by comparing the APB contrast in three dark field images realized in a two-beam geometry with the superstructure reflections (110), (210), and (120), as shown in Table I. A given APB is out of contrast in only one case and in contrast in the two others. In a previous work, it has been shown that the APB of Co-Pt alloys perfectly ordered in the $L1_2$ state obey well these contrast rules, and are therefore unambiguously identified.[5,6]

HREM images of the structures projected along the [001] cubic axis have been used in addition to the dark field images. Since the lattice parameter of both $L1_0$ and $L1_2$ is about 3.8 Å, we were limited to superstructure images obtained by selecting the {100} and {110} superstructure reflections with an objective aperture of 9 nm^{-1}.[14] The EMS code[15] has been used to simulate the patterns corresponding to our imaging conditions. As shown in Fig. 2, for wide ranges of thickness (4–20 nm) and (negative) defocus (60–120 nm), the HREM image of the $L1_2$ structure consists of a pattern formed by intense bright dots located on the Co-rich columns. HREM images of a $L1_0$ structure with a fourfold axis normal to the incident beam show regularly spaced fringes normal to the fourfold axis, and located above the Co-rich planes for the same range of thickness and defocus.

TABLE I. Contrasts in dark field images using superstructure reflections of a (001) zone.

	$L1_0$ structure			$L1_2$	APB in the $L1_2$ structure		
	X	Y	Z		$\mathbf{R}=\frac{1}{2}[011]$	$\mathbf{R}=\frac{1}{2}[101]$	$\mathbf{R}=\frac{1}{2}[110]$
(120) DF	white	black	black	gray	no contrast	black	black
(210) DF	black	white	black	gray	black	no contrast	black
(110) DF	black	black	white	gray	black	black	no contrast

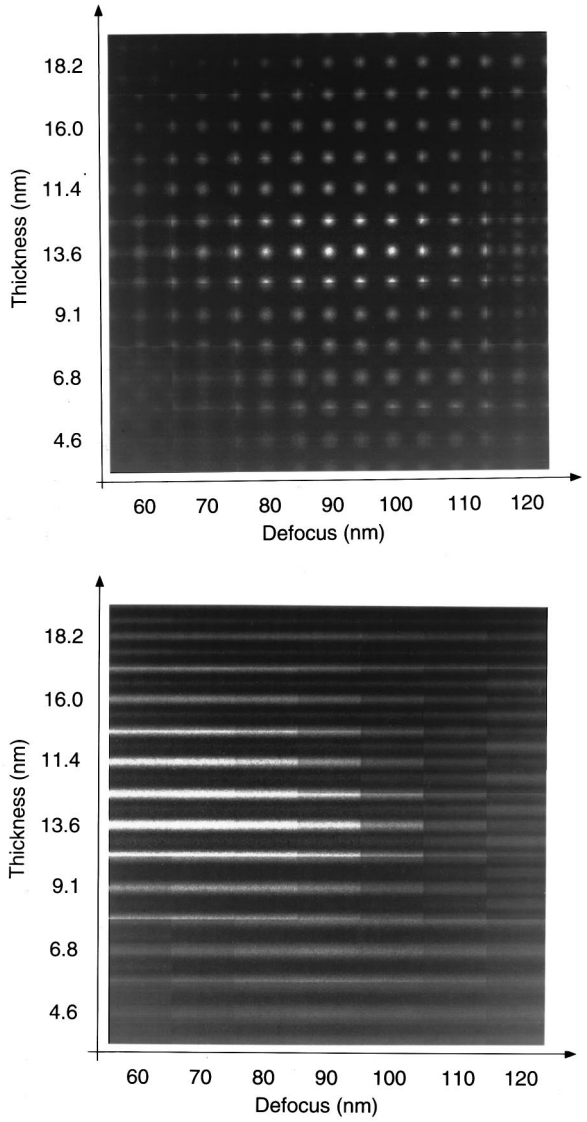

FIG. 2. Simulation maps of HREM images as a function of thickness and of the absolute value of the negative defocus: $L1_2(CoPt_3)$ structure (top) and $L1_0(CoPt)$ structure (bottom). For the $L1_0$ the tetragonal axis is along [010] (vertical axis).

This type of HREM images provides therefore a direct analysis of both the structure and the type of variant.

III. EXPERIMENTAL RESULTS

The phase diagram determined by Leroux *et al.*[11] was used to choose the alloy concentrations and annealing temperatures. Numerous samples with an atomic concentration of platinum ranging from 61.5 to 63% were prepared and first ordered in the $L1_2$ state. The annealing temperature was then progressively reduced down to a temperature close to the limit of the $L1_2+L1_0$ stability region. Thus, for $Co_{38.5}Pt_{61.5}$, $Co_{38}Pt_{62}$, $Co_{37}Pt_{63}$ the temperature at the end of the procedure described in Sec. II A were respectively 690, 600 and 550 °C.

Images of a typical microstructure are shown in Fig. 3. The microstructure consists of $L1_2$ domains separated by antiphase boundaries, but the antiphase boundaries are decorated. Indeed, by comparing the three dark fields (110), (210), and (120) of a [001] zone axis, we see that the APB obey exactly the contrast rules for $L1_0$-type ordering; an APB now appears with a dark contrast in two given DF and with a strong white contrast in the third one. The width of the $L1_0$ layer is about 4 nm. Furthermore, the dark field technique allows us to link the nature of the orientational $L1_0$ variant decorating the APB to the displacement vector of this APB. The results are summarized in Table II. It is clear from this table that the fourfold axis of the $L1_0$ phase is always normal to the displacement vector of the APB. This relationship has always been observed whatever the orientation of the APB. This is not enough to fully characterize the $L1_0$ variant that appears along the APB. We have also to determine which one, among the two possible translational variants, is formed. A very convenient way to get such an infor-

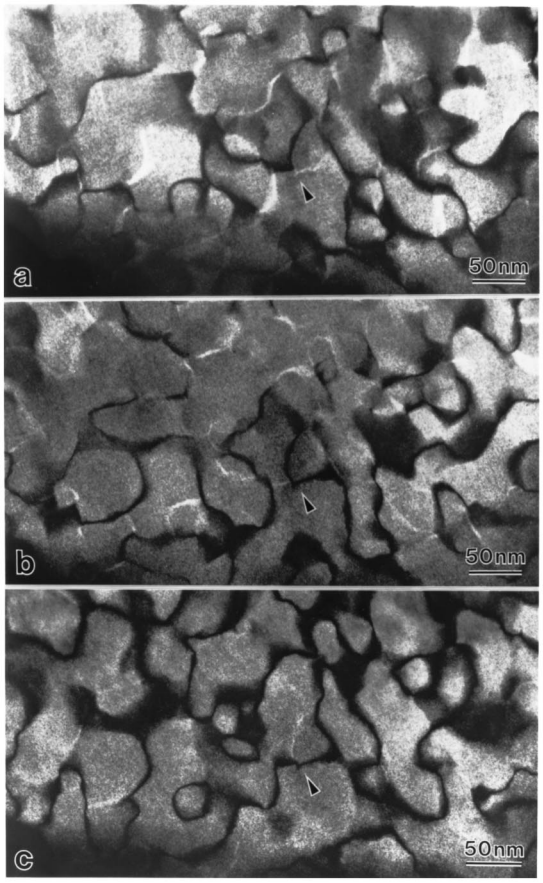

FIG. 3. Dark field images of APB in the $Co_{38.5}Pt_{61.5}$ aged at 690 °C: (a) (120), (b) (210), and (c) (110). The arrows indicates a junction of three APB, each one being decorated by a different $L1_0$ orientation variant.

TABLE II. Relation between the vector shift and the tetragonal axis of the wetting layer.

Displacement vector between the $L1_2$ variants	Tetragonal axis of the $L1_0$ structure
$\frac{1}{2}[011]$	[100]
$\frac{1}{2}[101]$	[010]
$\frac{1}{2}[110]$	[001]

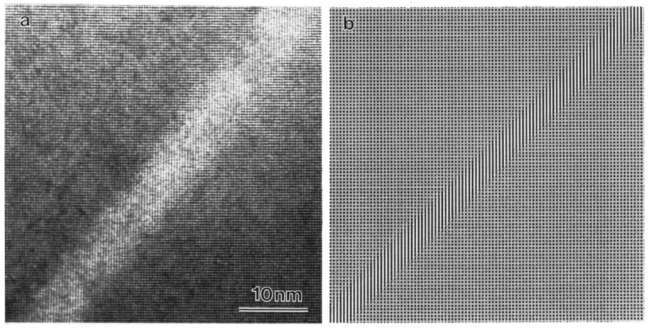

FIG. 4. (a) HREM image of a $Co_{38.5}Pt_{61.5}$ sample showing an APB (displacement vector $\mathbf{R}=1/2[011]$) decorated by the $L1_0$ variant having its tetragonal axis along [100] (horizontal axis). Note that the variant is such that the (100) platinum-rich planes are continuous from $L1_0$ to $L1_2$. (b) Mean field simulation of a flat APB normal to [110] with $\mathbf{R}=1/2[011]$, $T=4.5J_1/k_B$ and $(h-h_c)/J_1=7.1\,10^{-3}$.

mation is to take HREM images of the decorated APB with the foil normal oriented along the [001] direction. An example of a HREM image is presented in Fig. 4. We have compared our images with simulations patterns obtained with the EMS code. The result of our analysis is that the translational variant of the $L1_0$ structure formed during the wetting process is such that its platinum rich cubic planes are also platinum rich planes of the $L1_2$ structure. This result is sketched in Fig. 5. So both rotational and translational variants of the $L1_0$ structure are determined by the type of APB between the two $L1_2$ variants.

Finally, let us point out that in the first step of wetting in the Co-Pt system shown in Fig. 3, the APB are decorated but remain isotropic. Because the coherency strain between a tetragonal precipitate ($L1_0$) in a cubic matrix ($L1_2$) is highly anisotropic, this persistent isotropy proves that our assumption of a low strain energy is reliable, and that the main features of the wetting phenomenon in the Co-Pt system can be described using a theoretical approach based on short-ranged chemical interactions only.

IV. THEORETICAL MODELS

In this section, we develop different theoretical approaches in order to understand the origin of the selection of a single orientational and translational variant of the $L1_0$ structure along the antiphase boundaries, and to describe this peculiar wetting phenomenon.

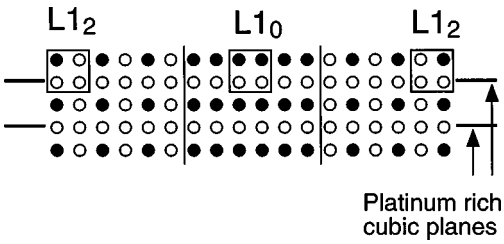

FIG. 5. Schematic representation of the decorated APB as observed in the Co-Pt samples from HREM images. Sketch of an APB in the $L1_2$ phase wetted by the $L1_0$ structure.

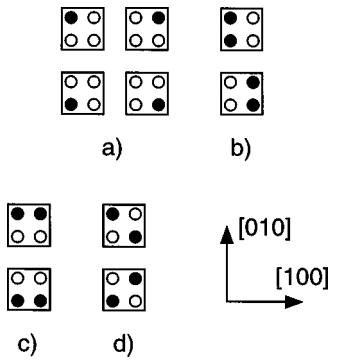

FIG. 6. Projection of the first nearest neighbor tetrahedra (a) $L1_2$; (b)–(d) $L1_0$ with a tetragonal axis along [100], [010], and [001], respectively.

A. Microscopic model at 0 K with interactions up to second nearest neighbors

The Ising model applies quite naturally to binary alloys where the two-valued spin variable denotes the nature of the atom at each site. The choice of such a Hamiltonian can be justified from the electronic structure of the alloy by using the so-called generalized perturbation method.[16] Our approach is limited to a perfect fcc lattice with interactions up to second nearest neighbors. The grand-canonical energy E can then be written as

$$E=\frac{1}{2}J_1\sum_{n,m}\sigma_n\sigma_m+\frac{1}{2}J_2\sum_{n,m}\sigma_n\sigma_m-h\sum_n\sigma_n, \quad (4.1)$$

where $\sigma_n=1$ when site n is occupied by an atom of cobalt and $\sigma_n=-1$ otherwise. The first and second sums run over the first and second nearest neighbors, respectively, and h plays the part of a chemical potential difference.

The fcc lattice can be decomposed into tetrahedra built on nearest neighbors. A conventional 2D representation of this lattice is a projection along the [001] direction of two successive (100) atomic planes. The first nearest-neighbor tetrahedra are then represented by squares. All possible tetrahedra are listed in Fig. 6. Let us consider an APB between two $L1_2$ variants wetted by the $L1_0$ structure. We first consider a flat APB normal to a cubic direction. The question is to know which $L1_0$ variant provides the minimum energy for a given APB. Within our simple approach limited to second nearest neighbors, the occurrence of a phase diagram involving the $L1_0$ and $L1_2$ phases (as observed in the Co-Pt system) requires a positive J_1 and a negative J_2. The homogeneous ground states of this model are well known (see for example Ref. 17). The results are recalled in Fig. 7. Because we are

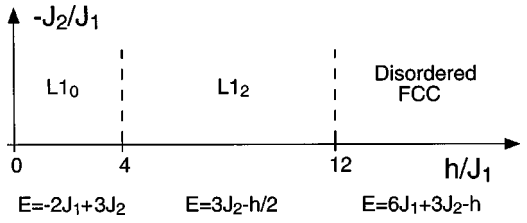

FIG. 7. Ground states and associated energies per site for the fcc lattice ($J_1>0$, $J_2<0$).

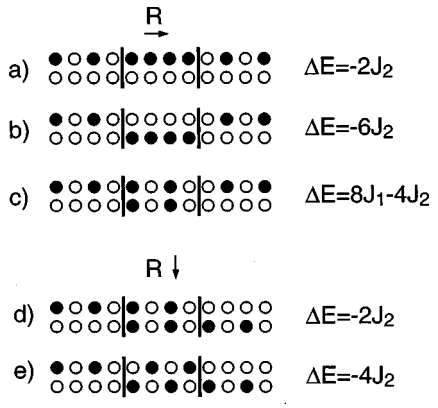

FIG. 8. Excess energy cost at $0K$ of different $L1_2$ APB configurations wetted by the $L1_0$ phase. (a)–(c) correspond to the same non conservative APB. (d), (e) illustrate the case of a conservative APB. Energies are given per site of a (100) plane parallel to the APB. (a) and (d) are the ground state structures for the translation vectors 1/2[101] and 1/2[011], respectively.

only interested in the $L1_2+L1_0$ stability region, the chemical potential h should be equal to $h_c=4J_1$.

As shown in Fig. 8, we have introduced a slice of $L1_0$ between two $L1_2$ domains. We have then calculated the energies of the two $L1_0/L1_2$ interfaces. All the possibilities for the $L1_0$ variant and for the position of the APB have been investigated. Only a few examples are shown in Fig. 8. It is easy to find a lower bound for the excess energy. Indeed, each $L1_2/L1_0$ interface induces an energy cost of at least $-J_2$ per site of a (100) plane parallel to the APB. The total free energy of an APB is then higher than $-2J_2$. A complete enumeration of the different configurations shows that, for a given displacement vector between the two $L1_2$ domains, this minimum is attained for a single configuration (see, for example, Fig. 8). Any other configuration presents a J_2 defect of higher energy and, in some cases, even a J_1 defect which has a high contribution to the excess energy. To test the influence of the APB orientation upon wetting, the same kind of analysis has been performed for an APB normal to a [110] direction. The minimum energy at 0 K is still provided by a unique $L1_0$ variant. These results are in full agreement with our experimental observations in the Co-Pt system.

We conclude that at low temperature, an APB between two $L1_2$ domains is expected to be wetted by only one type of $L1_0$ variant, whatever the value of J_1 and J_2 (provided that $J_1>0$ and $J_2<0$). This variant has its fourfold axis normal to the displacement vector and is exactly the one observed experimentally.

B. Wetting behavior: Mean field simulations

Many theoretical studies have been devoted to the wetting of interfaces. In the case of a scalar order parameter, a simple argument can be put forward to account for the wetting behavior. We recall it briefly.[2,10] In Fig. 9 are drawn the typical evolutions of the free energy and of the order parameter η close to the two-phase stability region. The excess free energy associated with a domain wall is written

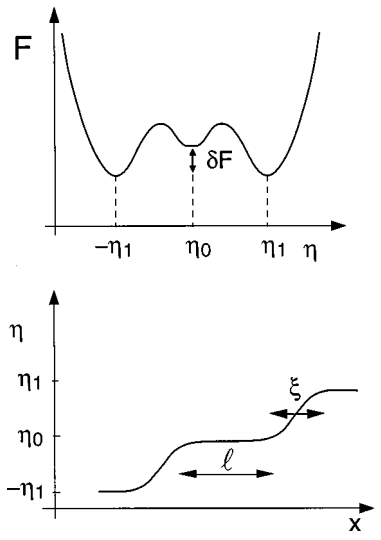

FIG. 9. Typical evolution of the free energy and of the order parameter during a wetting process for a first order transition. In the wetting limit, the width l of the wetting layer is much larger than the intrinsic width ξ of the partial interfaces.

$$\Delta F=\int_{-\infty}^{+\infty}\Delta F(x)dx=2F_{\mathrm{IPB}}+l\delta F+\alpha\exp(-l/\xi), \tag{4.2}$$

where l is the width of the wetting layer and ξ is the correlation length in the wetting structure. F_{IPB} and δF denote the interface energy and the excess free energy between the bulk and the wetting structures, respectively. The right hand side of Eq. (4.2) can be analyzed as the sum of three terms: (i) a constant term equal to twice the energy of an interface between the bulk structure and the wetting structure (ii) an attractive term due to the excess free energy δF of the structure created during the wetting process, (iii) a repulsive term due to the overlap of the two interfaces tails. It is easy to show that within a Ginzburg-Landau approach, this term is proportional to $\exp(-l/\xi)$.

Minimization of the free energy with respect to the width l gives the well known wetting law: $l\sim\xi\ln\delta F$. Even if the width l is the most natural parameter, it is not the easiest one to calculate. When the wetting layer is large enough, the excess concentration Δc of the minority species due to the interface is proportional to l. As Δc is very easily obtained from the numerical simulations, we have preferred to study the evolution of this quantity. It is worth mentioning that within this model, wetting is unavoidable because of the one-dimensional character of the order parameter. As discussed below, the relevant order parameter in our situation has in fact three components.

To analyze the thermodynamical behavior of the APB, we now start from our microscopic Ising model with interactions up to second nearest neighbors and use a mean field approach. We work within a grand-canonical ensemble; this is necessary to insure that the concentration within the $L1_2$ domains is asymptotically equal to its bulk value far away from the interface and then to calculate excess concentrations due to this interface. The mean field internal energy U is given by

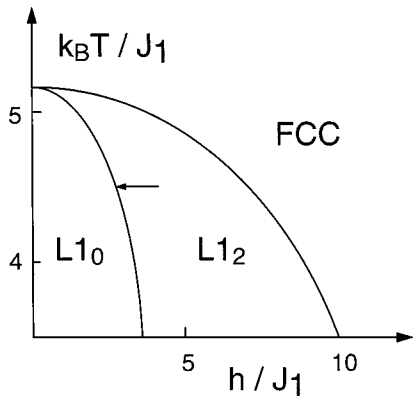

FIG. 10. Phase diagram for the fcc lattice obtained within the mean field approximation and for interactions up to second nearest neighbors. J_2/J_1 is equal to -0.2. The arrow indicates the path followed in the mean field simulation to reach the wetting regime.

$$U=\frac{1}{2}J_1\sum_{n,m}\langle\sigma_n\rangle\langle\sigma_m\rangle+\frac{1}{2}J_2\sum_{n,m}\langle\sigma_n\rangle\langle\sigma_m\rangle-h\sum_n\langle\sigma_n\rangle, \tag{4.3}$$

where the concentration of the minority species at site n is $c_n=(1+\langle\sigma_n\rangle)/2$. The numerical value of J_2 is set equal to $-J_1/5$ $(J_1>0)$, because in most binary alloys, first neighbors are expected to interact more strongly than second neighbors.

The corresponding phase diagram is shown in Fig. 10. For temperatures above $T_0=4J_1/k_B$, the only stable structures are $L1_0$, $L1_2$ and the disordered fcc. The L' structure, which is of no interest here, can only be stabilized for temperatures below T_0.[17] This mean field phase diagram is of course known to be fairly inaccurate, but since we are interested in the vicinity of the $L1_0-L1_2$ transition line, this is not a real problem here in consideration of the advantage of using a simple scheme. Using more accurate methods as the CVM or Monte Carlo simulations would not change qualitatively the results described below.[3]

The wetting phenomenon of antiphase boundaries in the $L1_2$ structure by the $L1_0$ structure is expected to occur when the system is brought closer and closer to the $L1_0$ stability region. Provided that the system is kept inside the $L1_2$ stability region, the precise nature of the path followed to reach a point of the two-phase region is irrelevant. For convenience, we have chosen a constant temperature $(T=4.5J_1/k_B)$, and we have varied the chemical potential. The corresponding path is sketched by an arrow in the phase diagram of Fig. 10.

The common way to proceed is to impose the presence of an APB within the simulation box and to minimize the free energy by using a second order algorithm. In the present paper, we have preferred to use a kinetic approach that consists in following the temporal evolution of an initially sharp APB. The corresponding kinetic mean field equations lead at long times to the equilibrium state. Particular attention has also been paid to the layering effect. Using a spin-flip dynamics with a transition probability W given by $W=\theta\exp(-\beta\Delta E/2)$, where θ is a flipping rate and ΔE the energy cost of a spin flip, the evolution of the mean magnetization $\langle\sigma_n\rangle$ is given by (see, for example, Ref. 18)

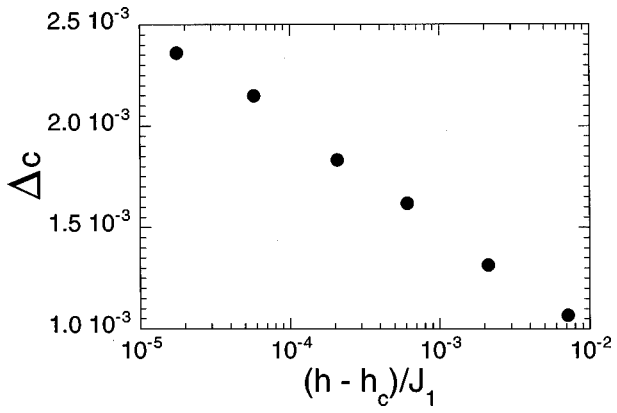

FIG. 11. Logarithmic divergence of the excess concentration Δc as a function of $(h-h_c)/J_1$.

$$\frac{d\langle\sigma_n\rangle}{dt}=-2\theta\{-\sinh\beta h_n^{\mathrm{eff}}+\langle\sigma_n\rangle\cosh\beta h_n^{\mathrm{eff}}\}, \tag{4.4}$$

where the local effective field h_n^{eff} is equal to $h-J_1\Sigma_m\langle\sigma_m\rangle-J_2\Sigma_m\langle\sigma_m\rangle$, the sums running over the first and second nearest neighbors of site n, respectively.

These kinetic equations lead to a path along which the free energy is decreasing. Indeed, it is easy to show that Eq. (4.4) implies

$$\frac{dF(\{\langle\sigma_n\rangle\},t)}{dt}\leqslant 0, \tag{4.5}$$

where $F(\{\langle\sigma_n\rangle\},t)$ is the mean field free energy:

$$F=U+k_BT\left\{\sum_n c_n\log c_n+(1-c_n)\log(1-c_n)\right\}, \tag{4.6}$$

and U is given by Eq. (4.3). It is then straightforward to integrate the kinetic equation (4.4), using a discrete time algorithm. We have used a first order scheme, which has the advantage of simplicity and, more importantly, to conserve the property (4.5).

We have first imposed translational invariance along the [010] and [001] directions. As the kinetic mean field equations conserve these invariances, the APB is necessarily normal to the [100] direction and flat. We can then reduce the computational box to a one-dimensional box of typically $200\times2\times2$ cubes. It is worth mentioning that this procedure prevents the occurrence of transverse fluctuations. So, this approach is only reasonable at low enough temperature, i.e., below the roughening transition,[19] where the transverse fluctuations are small. In order to use periodic boundary conditions, we have introduced in the computational box two APB associated with opposite displacement vectors.[2]

Our simulations show that the APB may indeed be wetted by the $L1_0$ phase whatever the displacement vector between the two $L1_2$ domains. As can be seen in Fig. 11, our mean field results for a [100] APB defined by the displacement vector 1/2 [110] and for $T=4.5J_1/k_B$ show a definite logarithmic divergence of the excess concentration Δc in the APB as a function of $(h-h_c)$. Furthermore, the $L1_0$ variant formed along the APB is found to be in full agreement with the experimental observations in the Co-Pt system, i.e., the

tetragonal axis of the $L1_0$ structure is always normal to the displacement vector and the selected translational variant insures the continuity of the ''pure planes'' from one structure to the other.

Finally, in order to evaluate the influence of the APB orientation on the wetting process, we have simulated domain walls in (110) planes. Due to the translational invariance along the [001] direction, a two-dimensional $100\times100\times2$ box can again be used. Periodic boundary conditions are chosen in the [001] direction. Along the other two cubic axis, the boundary conditions correspond to an infinite series of regularly spaced (110) domain walls. As in the [100] case, we observe a wetting phenomenon by a $L1_0$ variant [see Fig. 4(b)]. The rules governing the nature of the $L1_0$ variant are found similar for APB oriented in (110) and cubic planes. As observed experimentally in the Co-Pt system, these rules seem to be independent of the orientation of the antiphase boundary.

As mentioned previously, a first order transition leads always to a wetting phenomenon when the order parameter associated with this transition is scalar. This is not the case for the $L1_0-L1_2$ transition, as explained below. Yet, our mean field simulations show that the wetting phenomenon does occur, and that the divergence of the width of the wetting layer is still logarithmic. The type of variant formed along the APB is the same for APB parallel to the (100) and (110) planes and corresponds exactly to the experimental observations in the Co-Pt system.

C. Continuum model

The wetting behavior can be described using a phenomenological model where the local order parameter and the local concentration are treated within a Landau approach. This high temperature model will clearly demonstrate that the wetting of the APB in the $L1_2$ structure by the $L1_0$ phase is not unavoidable. Finally, being able to describe any flat APB, it incorporates automatically the symmetries of the underlying fcc lattice and will be used to test the anisotropy of the wetting phenomenon.

1. Order parameter for the $L1_2$ and $L1_0$ structures

Since the $L1_2$ and $L1_0$ structures are respectively fourfold and sixfold degenerated, the description of the domain walls requires a multidimensional order parameter. A very convenient method consists in introducing the concentration wave formulation which takes advantage of the superstructure periodicity.[21] If $c_{\mathbf{R}}$ denotes the concentration of the minority species at site R of the binary alloy, one can write

$$c_{\mathbf{R}}=c+\sum_{\mathbf{K}\neq0} c_{\mathbf{K}}\exp(i\mathbf{K}\cdot\mathbf{R}), \tag{4.7}$$

where c is the mean concentration and $\mathbf{K}$ is a vector of the reciprocal lattice vector belonging to the first Brillouin zone of the fcc structure. To describe the $L1_2$ and $L1_0$ structures, only the $\mathbf{K}$ vectors of type [100] need to be considered, so that[22]

$$c_{\mathbf{R}}=c+\eta_x\cos(\mathbf{k}_x\cdot\mathbf{R})+\eta_y\cos(\mathbf{k}_y\cdot\mathbf{R})+\eta_z\cos(\mathbf{k}_z\cdot\mathbf{R}), \tag{4.8}$$

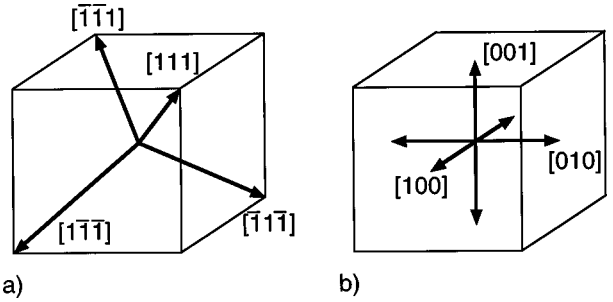

FIG. 12. Sketch of the three-dimensional order parameter. (a) $L1_2$ structure, (b) $L1_0$ structure.

where $\mathbf{k}_x=2\pi/a[100]$, $\mathbf{k}_y=2\pi/a[010]$, and $\mathbf{k}_z=2\pi/a[001]$. $\boldsymbol{\eta}=(\eta_x,\eta_y,\eta_z)$ is the three-dimensional order parameter. Because $c_{\mathbf{R}}$ has to be positive and smaller than one, $\boldsymbol{\eta}$ should belong to the polyhedron defined by the following inequalities:

$$\begin{aligned}
&-c\leqslant\eta_x+\eta_y+\eta_z\leqslant(1-c),\\
&-c\leqslant\eta_x-\eta_y-\eta_z\leqslant(1-c),\\
&-c\leqslant-\eta_x+\eta_y-\eta_z\leqslant(1-c),\\
&-c\leqslant-\eta_x-\eta_y+\eta_z\leqslant(1-c).
\end{aligned} \tag{4.9}$$

In this formalism, the origin ($\boldsymbol{\eta}=0$) represents the disordered phase, where all sites are occupied with the same probability. The six possible $L1_0$ variants correspond to the six cubic semiaxes: $\boldsymbol{\eta}=\pm\eta[100],\pm\eta[010],\pm\eta[001]$. Similarly, the four translational variants of the $L1_2$ structure (with the same stoichiometry A_3B) are represented by $\boldsymbol{\eta}=\eta[111]$, $\eta[\bar{1}\bar{1}1]$, $\eta[\bar{1}1\bar{1}]$, and $\eta[1\bar{1}\bar{1}]$ in $\boldsymbol{\eta}$ space.[17,4] A representation of the $L1_0$ and $L1_2$ variants in the (long range order) parameter space is shown in Fig. 12.

One can therefore describe the variants of $L1_0$ and $L1_2$ structures within the same formalism, using the three-dimensional order parameter $\boldsymbol{\eta}$. The rules determining the $L1_0$ variant formed during the wetting process appear also quite naturally in this order parameter space. The direction of the order parameter characterizing the (rotational and translational) variant of the $L1_0$ structure lies indeed just in between the directions of the order parameters characterizing the two $L1_2$ bulk structures.

2. Landau expansion for an homogeneous system

Within the Landau theory, we compare the free energy F of an ordered state with that of the disordered state and perform an expansion as a function of the components of the order parameter, taking due account of the cubic symmetry.

$$\delta F_{\mathrm{hom}}=\frac{1}{2}r\Sigma_k\eta_k^2+w\,\eta_1\eta_2\eta_3+\frac{1}{4}u(\Sigma_k\eta_k^2)^2+\frac{1}{4}v\Sigma_k\eta_k^4+\cdots. \tag{4.10}$$

A fourth order expansion is sufficient to describe the $L1_2\rightarrow L1_0$ first order transition. With the requirements $u+v>0$, $3u+v>0$, and $r<0$, the local minima of the free en-

ergy expansion correspond indeed either to the $L1_2$ or to the $L1_0$ phase. An expansion up to sixth order with $u+v<0$ would be necessary to describe the first order transition between the $L1_0$ and the fcc solid solution.

3. Ginzburg-Landau functional for an heterogeneous system

We focus here on the specific heterogeneity of a flat interface between two different $L1_2$ domains. From a thermodynamical point of view, a planar domain wall forced by appropriate boundary conditions is stable. Then, by comparing with an homogeneous system, the excess interface free energy, entropy, etc., can be defined properly. Let us consider a flat interface normal to the vector $\boldsymbol{\rho}$. The problem is to determine the profile $\phi(x)=\phi[c(x),\boldsymbol{\eta}(x)]$ where x is the coordinate normal to the interface. We then assume that $c(x)$ varies much more slowly than $\eta(x)$ and neglect its spatial dependence. The definition of $\eta_\alpha(x)$ requires some coarse grain average, so that the order parameter is only defined on a scale large enough compared to the relevant unit cell. It is therefore assumed that $\eta_\alpha(x)$ does not vary too rapidly. As a consequence, a first local contribution to the heterogeneous free energy is simply the energy calculated for the local value of $\eta_\alpha(x)$. On the other hand, the spatial variation of the order parameter has an energy cost and the simplest approximation is to include first order derivatives only, which yields the well-known Landau-Ginzburg free energy functional $\mathcal{F}$[20,21]

$$\mathcal{F}=\int_{-\infty}^{+\infty} dx/a\left[F_{\mathrm{hom}}(x)+\frac{1}{2}\sum_\alpha m_\alpha(d\eta_\alpha/dx)^2\right], \tag{4.11}$$

where the m_α are positive constants. This phenomenological model can also be derived as a continuous limit of the mean field free energy (4.6). The link between these two approaches allows us to express the phenomenological parameters of the Ginzburg Landau free energy functional expression in terms of c,T, the microscopic interactions and the lattice parameter a:

$$\begin{aligned} r&=16\left[(-4J_1+6J_2)+\frac{1}{4}k_BT\left(\frac{1}{c}+\frac{1}{1-c}\right)\right],\\ w&=-4k_BT\left(\frac{1}{c^2}-\frac{1}{(1-c)^2}\right),\\ u&=4k_BT\left(\frac{1}{c^3}+\frac{1}{(1-c)^3}\right),\\ v&=-\frac{2}{3}u,\\ m_\alpha&=8a^2(J_1\rho_\alpha^2-J_2), \end{aligned} \tag{4.12}$$

where the ρ_α are the coordinates of the vector $\boldsymbol{\rho}$ normal to the interface.

4. Equilibrium equations and mechanical analogy

Taking the functional derivative of Eq. (4.11) with respect to the order parameters gives the equilibrium equations for these parameters or APB profiles $\eta_\alpha(x)$:

$$\begin{aligned} m_1d^2\eta_1/dx^2&=r\eta_1+w\eta_2\eta_3+u\eta_1(\eta_1^2+\eta_2^2+\eta_3^2)+v\eta_1^3,\\ m_2d^2\eta_2/dx^2&=r\eta_2+w\eta_1\eta_3+u\eta_2(\eta_1^2+\eta_2^2+\eta_3^2)+v\eta_2^3,\\ m_3d^2\eta_3/dx^2&=r\eta_3+w\eta_1\eta_2+u\eta_3(\eta_1^2+\eta_2^2+\eta_3^2)+v\eta_3^3. \end{aligned} \tag{4.13}$$

With proper boundary conditions, this set of non-linear coupled differential equations completely defines the evolution of the order parameter across the APB. As is well known the underlying mathematics of the minimization of the functional (4.11) are equivalent to a classical mechanic problem if we identify $1/2\Sigma_\alpha m_\alpha(d\eta_\alpha/dx)^2$ with a kinetic energy and $-F_{\mathrm{hom}}$ with a potential energy.[21] Within this analogy, x plays the part of time, η of the position and m_α of the diagonal mass tensor. Finally, the first integral of the system (4.13) corresponding to the conservation of the total energy is given by

$$\begin{aligned} &\frac{1}{2}\Sigma_\alpha m_\alpha(d\eta_\alpha/dx)^2-F_{\mathrm{hom}}[\eta_1(x),\eta_2(x),\eta_3(x)]\\ &\quad=-F_{\mathrm{hom}}(\eta_{\mathrm{eq}},\eta_{\mathrm{eq}},\eta_{\mathrm{eq}}). \end{aligned} \tag{4.14}$$

However, since the potential energy is of the opposite sign of F_{hom}, the equilibrium values of $\eta(x)$ correspond here to maxima and not to minima of this potential energy. The profile of an APB between two $L1_2$ domains is thus equivalent to the path followed by a ball of mass (m_1,m_2,m_3) rolling on the hypersurface $-f(\eta_1,\eta_2,\eta_3)$. The shape of this hypersurface is shown in Fig. 13 where we have assumed $\eta_2=\eta_3$ for simplicity. The ball starts from the top of the hill corresponding to the equilibrium bulk order parameter $(\eta_{\mathrm{eq}},\eta_{\mathrm{eq}},\eta_{\mathrm{eq}})$ with an infinitesimal velocity and rolls up to the top of the $(\eta_{\mathrm{eq}},-\eta_{\mathrm{eq}},-\eta_{\mathrm{eq}})$ hill. The highest hills correspond to the stable phase $L1_2$, whereas the other represents the metastable phase $L1_0$. Near the $L1_0$ stability region in the phase diagram, the difference between the heights of the $L1_2$ and $L1_0$ hills is small. In that case, if the ball rolls close to the top of the $L1_0$ hill, it will slow down and a wetting phenomenon will occur, but the ball may also follow a path which avoids the $L1_0$ hill. As a consequence, the wetting phenomenon of an APB may not occur when the order parameter has several components.

5. Equilibrium antiphase boundary in the $L1_2$ structure

Without loss of generality, we consider an APB between two ordered domains shifted by a vector $\mathbf{R}_{\mathrm{APB}}=1/2[011]$. We impose the following boundary conditions:

$$\begin{aligned} &\eta_1(x)\to+\eta_{\mathrm{eq}},\quad \eta_2(x)\to-\eta_{\mathrm{eq}},\quad \eta_3(x)\to-\eta_{\mathrm{eq}}\\ &\qquad\text{when}\quad x\to-\infty,\\ &\eta_1(x)\to+\eta_{\mathrm{eq}},\quad \eta_2(x)\to+\eta_{\mathrm{eq}},\quad \eta_3(x)\to+\eta_{\mathrm{eq}}\\ &\qquad\text{when}\quad x\to+\infty, \end{aligned} \tag{4.15}$$

where $\boldsymbol{\eta}=\eta_{\mathrm{eq}}(1,1,1)$ is an equilibrium value for the order parameter of the $L1_2$ phase. Solutions of Eq. (4.13) in which η_2 and η_3 are odd functions of x, and η_1 is even satisfy

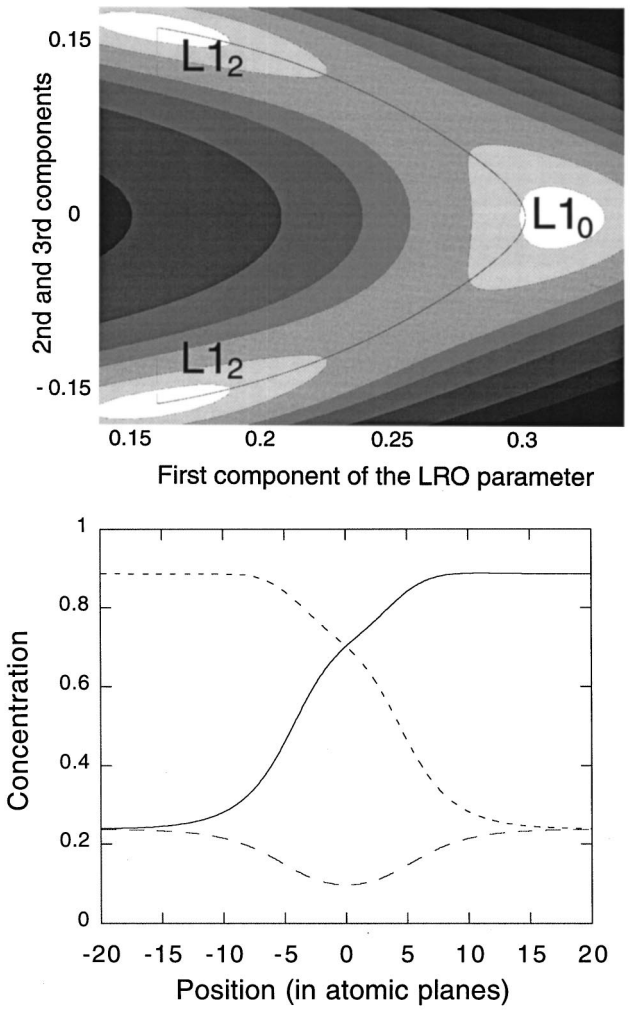

FIG. 13. Shape of the free energy hypersurface when $c=0.4$ and $T-T_c=1.077\times10^{-3}$ (upper part of the figure). The path corresponding to a flat APB normal to [100] is indicated. The continuous, dashed, and long-dashed curves in the lower part are the concentration profiles of the four sublattices c_0, c_1, and $c_2=c_3$ across the APB.

these conditions. The equilibrium equations can then be solved on the semi-infinite interval $[0,+\infty[$ with the new boundary conditions

$$\eta_1'(0)=0,\quad \eta_2(0)=0,\quad \eta_3(0)=0,$$

$$\eta_1(x)\rightarrow+\eta_{\mathrm{eq}},\quad \eta_2(x)\rightarrow+\eta_{\mathrm{eq}},\quad \eta_3(x)\rightarrow+\eta_{\mathrm{eq}}$$
$$\text{when}\quad x\rightarrow+\infty. \tag{4.16}$$

The system (4.13) with these boundary conditions is then solved using a ''shooting'' algorithm.[23] The first step consists in guessing values for $\eta_2'(0)$ and $\eta_3'(0)$. The value of $\eta_1(0)$ is computed with the conservation of energy (4.14). Then the equilibrium equations are solved numerically with a Runge-Kutta algorithm. If the computed solution does not fulfill conditions (4.16), the initial guesses are corrected. Then, the equilibrium equations are solved once again, and this procedure is iterated up to reach a satisfactory agreement with conditions (4.16). In our work, the initial values of $\eta_2'(0)$ and $\eta_3'(0)$ are computed with an accuracy better than 10^{-8}.

We have investigated the case of a flat conservative APB, i.e., an APB for which the vector $\mathbf{R}_{\mathrm{APB}}=1/2[011]$ lies within the plane of the APB. So the second and third coordinates of the vector $\boldsymbol{\rho}$ normal to the flat APB are equal. The relation (4.12) implies that $m_2=m_3$ and the governing equations are now symmetric with respect to the interchange $\eta_2\leftrightarrow\eta_3$. Because the boundary conditions do not break this symmetry, the system (4.13) has a stationary solution where $\eta_2(x)=\eta_3(x)$. In this case, only one initial value has to be guessed and the shooting algorithm is more efficient. Moreover, the path across the APB (in the order parameter space) can easily be visualized (Fig. 13).

We have first performed a series of calculations for the [100] APB. All coefficients of the free energy functional are selected using the continuum limit of the mean field model (4.12). To compare this continuum approach with the mean field results of the previous section, we have chosen the same interaction coefficients J_1 and $J_2=-J_1/5$. The concentration is set equal to 0.4. The critical temperature below which the $L1_0$ phase is stable is $k_BT_c/J_1=4.2919$. The concentrations of the four cubic sublattices and the corresponding path in the order parameter space when $k_B(T-T_c)/J_1=1.077\times10^{-3}$ are shown in Fig. 13. It can be seen that an intervening $L1_0$-like layer begins to form along the APB. The width l of this layer increases when $T-T_c$ decreases. As in the scalar order parameter case, we expect l to diverge as $\ln\delta F$, or equivalently that the internal energy U_{APB} diverges as $\ln(T-T_c)$. We have found this logarithmic divergence of the internal energy for $k_B(T-T_c)/J_1$ in the range 10^{-1}–10^{-5}.

Attempts to calculate the profile of the APB closer to T_c leads to thicker layers together with a lower accuracy. In fact, the shooting method is an iterative process which amplifies the initial error on the initial coefficients $\eta_2'(0)$ and $\eta_3'(0)$. We found that the accuracy of 10^{-8} for the initial coefficients leads to a relevant profile on only 50 atomic planes. More detailed investigations would require using another type of algorithm such as the ''relaxation'' method.[23]

Finally, the influence of the orientation of the flat APB on the wetting behavior has been investigated. The continuum model presented in this section has the advantage that the anisotropy is introduced in a natural way and that it incorporates correctly the crystal symmetry of the fcc lattice. Since the continuous limit (4.12) gives an analytical expression for the gradient coefficients $m_\alpha(\boldsymbol{\rho})$, the profile of an APB can be easily computed for any orientation. Under the same conditions [$c=0.4$, $k_B(T-T_c)/J_1=7.745\,10^{-5}$], we have measured the width of the wetting layer defined as the distance between the two inflection points of the $\eta_1(x)$ curve. While the $L1_0$ layer is only 7 atomic planes wide for $\boldsymbol{\rho}=[100]$, it grows up to 13, 19, and 22 planes for the [411], [111], and [011] orientations, respectively. Our results show a strong anisotropy of the wetting behavior of an APB in the $L1_2$ phase by the $L1_0$ ordered phase. This result is similar to previous investigations on the fcc lattice where the wetting of the APB in the $L1_2$ phase by the disordered solid solution was also shown to be highly anisotropic.[24]

From the previous discussion it is clear that the wetting behavior of the APB in the $L1_2$ phase by the $L1_0$ ordered structure is not unavoidable. Nevertheless, in our computations at $c=0.4$ for several orientations a $L1_0$ layer is formed and the classical wetting law $U_{\mathrm{APB}} \sim \ln(T-T_c)$ still holds. Finally, because the above continuum model reproduces correctly the inherent anisotropy of the fcc lattice, the wetting behavior by the $L1_0$ ordered phase was shown to be highly anisotropic.

V. CONCLUSION

To summarize, the microscopic model based on the Ising model as well as the more general Landau-Ginzburg approach do account for the observed wetting by the $L1_0$ phase of APB in $L1_2$ close to the $L1_0-L1_2$ two-phase field. This justifies in a precise manner the widespread statement that new phases nucleate preferentially at defects. Actually, the Landau-Ginzburg approach shows that this is not always necessary the case, because of the multidimensional character of the relevant order parameter. Nevertheless here, for all values of the microscopic parameters consistent with a reasonable phase diagram, wetting has always been found to occur.

Although detailed investigations remain to be made, the anisotropy of the wetting phenomena predicted by the latter approach has not been observed till now. It might be that the microscopic model with only first and second neighbor interactions is not accurate enough here.

Complementary investigations[25] will be presented elsewhere. For example, it has been observed that elastic effects become important for thicknesses of the $L1_0$ wetting layers above 5 nm. These layers transform into platelets with well-defined orientations; this can be understood by taking elastic strains into account, the analysis being similar to that used to describe the chessboard patterns observed in Co-Pt samples annealed within the $L1_0-L1_2$ two-phase field.[26] Preliminary theoretical studies also indicate that the APB should behave differently at higher temperature, close to the triple point separating $L1_0$,$L1_2$ and the disordered phases where wetting by $L1_0$ and by the disordered phase compete.

ACKNOWLEDGMENTS

The authors would like to thank G. Schmerber and Dr. V. Pierron-Bohnes of the University of Strasbourg I (France) and D. Regen (ONERA) for their help in preparing the Co-Pt samples.

[1] R. Kikuchi and J. W. Cahn, Acta Metall. **24**, 1337 (1979).
[2] A. Finel, V. Mazauric, and F. Ducastelle, Phys. Rev. Lett. **65**, 1016 (1990).
[3] A. Finel, in *Ordering and Disordering in Alloys*, edited by A. R. Yavari (Elsevier Applied Science, London, 1992), p. 182.
[4] V. Mazauric, J. Comput.-Aided Mater. Des. **4**, 113 (1997).
[5] C. Leroux, Europhys. Lett. **12**, 155 (1990).
[6] C. Leroux, A. Loiseau, M. C. Cadeville, D. Broddin, and G. Van Tendeloo, J. Phys.: Condens. Matter **2**, 3479 (1990).
[7] C. Ricolleau, A. Loiseau, F. Ducastelle, and R. Caudron, Phys. Rev. Lett. **68**, 3591 (1992).
[8] A. Loiseau, Curr. Opin. Solid State Mater. Sci. **1**, 369 (1996).
[9] A. Loiseau, C. Ricolleau, L. Potez, and F. Ducastelle, in *Solid-Solid Phase Transformations*, edited by W. C. Johnson, J. M. Howe, D. E. Mc Laughlin, and W. A. Soffa (The MMM Society, Warrendale, 1994), p. 385.
[10] F. Ducastelle, C. Ricolleau, and A. Loiseau, Mater. Sci. Forum **155-156**, 367 (1994).
[11] C. Leroux, A. Loiseau, D. Broddin, and G. Van Tendeloo, Philos. Mag. B **1**, 57 (1991).
[12] C. Leroux, Thèse de Doctorat, Université de Strasbourg I, 1989.
[13] P. B. Hirsch, A. Howie, R. B. Nicholson, D. W. Pashley, and J. M. Whelan, *Electron Microscopy of Thin Crystals* (Butterworths, London, 1967).
[14] L. Potez and A. Loiseau, Interface Sci. **2**, 91 (1994).
[15] P. Stadelmann, Ultramicroscopy **21**, 131 (1987).
[16] F. Ducastelle, in *Alloy Phase Stability*, Vol. 163 of *Nato Advanced Study Institute, Series E: Applied Sciences*, edited by G. M. Stocks and A. Gonis (Kluwer, Dordrecht, 1989), p. 293.
[17] F. Ducastelle, *Order and Phase Stability in Alloys* (North-Holland, Amsterdam, 1991).
[18] F. Ducastelle, in *Theory and Applications of the Cluster Variation and Path Probability Methods*, edited by J. L. Moran-Lopez and J. M. Sanchez (Plenum Press, New York, 1996), p. 21.
[19] T. Saha-Dasgupta and A. Finel, in *Properties of Complex Inorganic Solids*, edited by A. Gonis, A. Meike, and P. E. A. Turchi (Plenum Press, New York, 1997), p. 121.
[20] K. Binder, in *Phase Transition and Critical Phenomena*, edited by C. Domb and J. L. Lebowitz (Academic Press, New York, 1983), Vol. 2.
[21] A. G. Khachaturyan, *The Theory of Structural Transformations in Solids* (Wiley, New York, 1983).
[22] Z.-W. Lai, Phys. Rev. B **41**, 9239 (1990).
[23] W. Press, B. Flannery, S. Teukolsky, and W. Vetterling, *Numerical Recipies* (Cambridge University Press, Cambridge, 1986).
[24] R. J. Braun, J. W. Cahn, G. B. McFadden, and A. A. Wheeler, Philos. Trans. R. Soc. London, Ser. A **355**, 1787 (1997).
[25] Y. Le Bouar, Thèse de Doctorat, Ecole Polytechnique, 1998.
[26] Y. Le Bouar, A. Loiseau, and A. G. Khachaturyan, Acta Mater. **46**, 2777 (1998).